

Highly Stable Zero-Dimensional Lead-Free Metal Halides for X-ray Imaging

Joo Hyeong Han, Tuhin Samanta, Yong Min Park, Ha Jun Kim, Noolu Srinivasa Manikanta Viswanath, Hyeon Woo Kim, Bo Kyung Cha, Sung Beom Cho,* and Won Bin Im*



Cite This: *ACS Energy Lett.* 2023, 8, 545–552



Read Online

ACCESS |

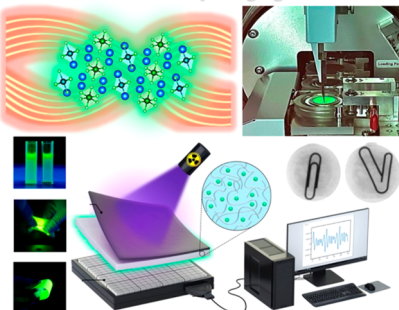
Metrics & More

Article Recommendations

Supporting Information

ABSTRACT: Scintillators are widely used for radiation detection in various fields, such as medical imaging, nondestructive testing, and crystallography. X-ray-generating systems typically emit large amounts of heat and require a high thermal stability of scintillators, particularly for nondestructive testing or radiation detection performed under harsh conditions. Therefore, highly stable scintillators must be developed for application in extreme environments. Herein, we developed new zero-dimensional lead-free monoclinic phases of Cs_3TbCl_6 and Rb_3TbCl_6 metal halides that are thermally and chemically stable. Cs_3TbCl_6 and Rb_3TbCl_6 polycrystals exhibit high light yields of 56800 and 88800 photons/MeV, respectively. Cs_3TbCl_6 and Rb_3TbCl_6 polycrystals also show low detection limits of 149.65 and 115.38 nGyairs⁻¹ due to their structural-optical properties, respectively. Furthermore, the fabricated thick films of Cs_3TbCl_6 and Rb_3TbCl_6 are applied to our homemade X-ray imaging system, and preferable spatial resolutions are obtained as compared with a commercial $\text{Gd}_2\text{O}_2\text{S}:\text{Tb}^{3+}$ film.

Thermally stable 0-D lead-free metal halides for X-ray imaging



Scintillators that convert high-energy photons (such as X-rays) to low-energy visible photons have become crucial for a wide range of applications, including medical diagnostic imaging, nondestructive testing, crystallography, quality inspection, security, etc. Materials such as CsI (CsI:TI), LYSO ($\text{Lu},\text{Y}_{2}\text{SiO}_5:\text{Ce}^{3+}$), and GOS ($\text{Gd}_2\text{O}_2\text{S}:\text{Tb}^{3+}$) are currently widely used as scintillators in indirect X-ray detectors.^{1–4} However, they have several limitations such as complicated synthesis processes and poor thermal stability.^{5–7} Recently, lead halide perovskites (LHPs) have attracted significant attention as scintillators due to their low detection limits and the possibility of multicolor radioluminescence (RL).^{8–12} However, the main drawbacks of the LHPs as scintillators are low thermal and chemical stability and self-absorption properties of LHPs. Moreover, the inherent toxicity of lead is a critical limitation of LHPs.^{13–16} Recently, lead-free metal halides have been developed as scintillators.^{17,18} For instance, Yang et al. reported that Rb_2CuBr_3 was as a scintillator with a high light yield¹⁹ and Zhang et al. applied Rb_2AgBr_3 , with its short scintillation decay time, to dynamic X-ray imaging.²⁰ In addition, Jiang et al. applied $\text{C}_4\text{H}_{12}\text{NMnCl}_3$ and $(\text{C}_8\text{H}_{20}\text{N})_2\text{MnBr}_4$ for a WLED and X-ray scintillator.²¹ Recently, Tb^{3+} -doped metal halides have attracted attention due to their interesting luminescence properties. Liu et al. reported persistent radioluminescence and excellent X-ray imaging using $\text{NaLuF}_4:\text{Tb}^{3+}$.^{22,23} However, despite these excellent findings, no studies have been able to overcome the

thermal quenching (TQ) problem. Therefore, developing scintillators that are nontoxic and stable at high temperatures and exhibit tiny changes in light yield with temperature is necessary.²⁴

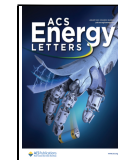
Herein, we report lead-free zero-dimensional (0D) monoclinic Cs_3TbCl_6 (CTC) and Rb_3TbCl_6 (RTC) as new scintillators with excellent thermal and chemical stabilities and bright green luminescence. Moreover, the two scintillators exhibited high light yields of 56800 and 88800 photons/MeV, low detection limits of 149.65 and 115.38 nGyairs⁻¹, robust X-ray radiation resistance, and higher spatial resolution, respectively, as compared with the commercial GOS scintillator film used in X-ray imaging.

CTC and RTC possess 0D crystal structures with a monoclinic space group of $\text{C}2/\text{c}$ (Figure 1a). Each Tb atom is bonded with six Cl atoms and forms octahedra. Moreover, it has two distinct Tb octahedra as shown in Figure 1b, and the corresponding bond lengths are shown in Figure S1 in the Supporting Information. To understand the electronic structures of CTC and RTC, we investigated their partial

Received: November 1, 2022

Accepted: December 7, 2022

Published: December 15, 2022



ACS Publications

© 2022 American Chemical Society

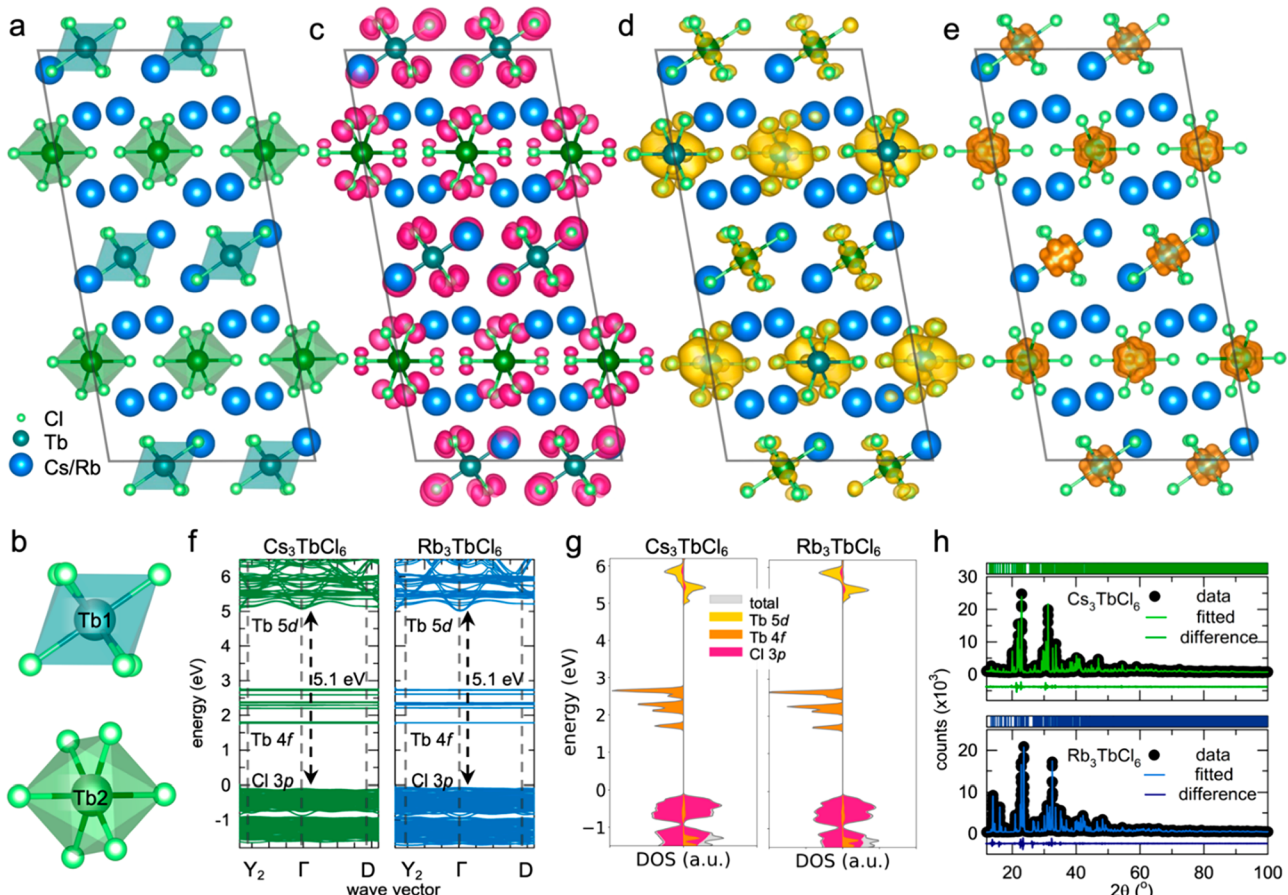


Figure 1. Structural properties of CTC and RTC: (a) crystal structures of CTC and RTC in the [010] direction; (b) illustrations of the different crystallographic sites of Tb atoms, respectively; (c–e) partial charge density of Cl 3p, Tb 5d, and 4f orbitals in CTC, respectively; (f) calculated electronic band structures of CTC and RTC; (g) density of states of CTC and RTC; (h) Rietveld refinement X-ray diffraction plots of CTC and RTC.

charge density, the orbital-projected density of states, and the electronic band structure (Figure 1c–g). As shown in Figure 1c, the charges of the Cl 3p orbitals, which mainly contribute to the valence band state, are distributed at the edge of [TbCl₆]³⁻ octahedra. The charges of the Tb orbitals are shown in Figure 1d,e. Tb 5d orbitals, which mainly contribute to the conduction band state, are distributed around [TbCl₆]³⁻ octahedra. The 4f orbitals of Tb³⁺ ions are distributed around the Tb atom in [TbCl₆]³⁻ octahedra, which are located between the band gap.

The overall orbital-projected density of states and the electronic band structures are shown in Figure 1f,g. Cs and Rb cations have a negligible influence on the frontier orbitals. Both CTC and RTC exhibit a direct band gap of 5.1 eV at the Γ point. This observed band gap was consistent with the experimental band gap calculated from the UV-vis reflectance spectrum using the Kubelka–Munk and Tauc equations (Figure S2 in the Supporting Information)^{25,26}. A Rietveld refinement was performed to determine the phase purity of the synthesized CTC and RTC (Figure 1h). The obtained results show the as-synthesized samples form without any secondary phases. The refined lattice parameters and atomic positions of CTC and RTC are given in Tables S1–S4 in the Supporting Information. The chemical nature of CTC and RTC was confirmed using X-ray photoelectron spectroscopy (XPS) (Figures S3a,d in the Supporting Information). The high-resolution XPS spectra of Tb 3d_{5/2}, Tb 3d_{3/2}, and Tb 4d_{5/2} of

CTC and RTC are shown in Figures S3b,c,e,f in the Supporting Information, respectively.

Further, we investigated the optical properties of CTC and RTC polycrystals (PCs). The steady-state photoluminescence (PL) and photoluminescence excitation (PLE) spectra of CTC and RTC PCs were measured upon 280 nm excitation and by monitoring the 548 nm emission, which is shown in Figure 2a. Upon 280 nm excitation, CTC and RTC exhibited bright green emission of Tb³⁺ ions at 548 nm, which is attributed to the ⁵D₄ → ⁷F₅ transition. The broad band ranges from 250 to 300 nm, corresponding to the charge transfer band (CTB) of Cl⁻ → Tb³⁺, with a maximum peak at 280 nm.^{27,28} The narrow bands ranging from 300 to 400 nm are assigned to the spin-forbidden 4f–4f transitions of the Tb³⁺ ions. The detailed luminescence mechanism of CTC and RTC is shown in Figure 2b. These energy levels are well-matched to the density of state results and reflectance spectra (Figure 1g and Figure S2 in the Supporting Information). Time-resolved PL spectroscopy of CTC and RTC polycrystals was also performed under an excitation of 280 nm at room temperature (Figure 2c). A single-exponential fit to the PL decay curve indicates that the emission occurs at a single luminescent center. CTC and RTC have lifetime values of 5.23 and 4.38 ms, respectively. Additionally, to evaluate the chemical stabilities of CTC and RTC in the ambient atmosphere, the XRD and PL of CTC and RTC PCs were measured for 3 months as a function of exposure time. The XRD and PL spectra show no significant

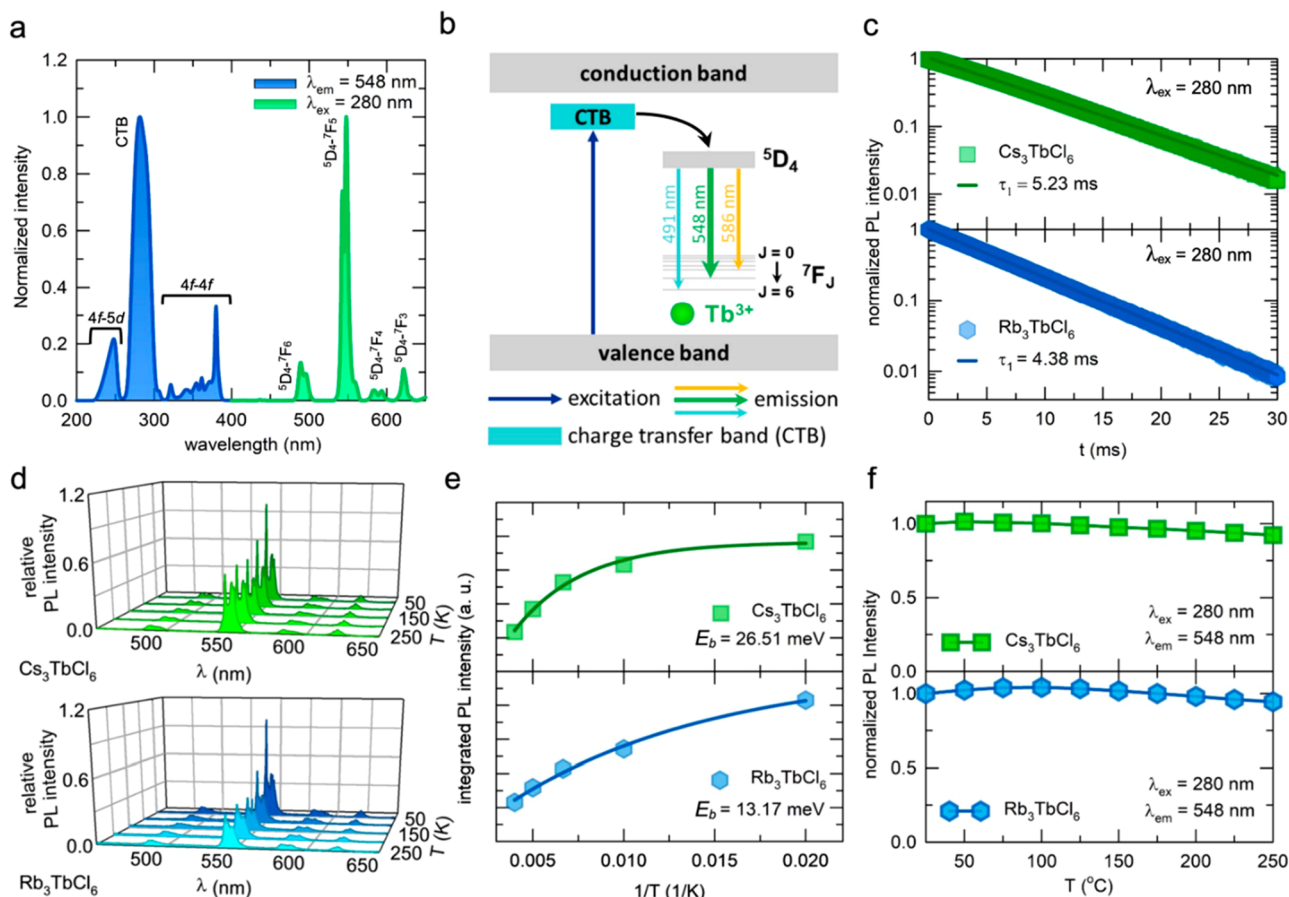


Figure 2. Luminescence properties of CTC and RTC: (a) PL and PLE spectra of CTC and RTC; (b) schematic illustration of the luminescence mechanism of CTC and RTC; (c) time-resolved PL of CTC and RTC; (d) low-temperature PL spectra of CTC and RTC; (e) Arrhenius plots to determine the exciton binding energy of CTC and RTC; (f) temperature-dependent PL of CTC and RTC in the range of 25–250 °C.

changes, which indicates that CTC and RTC have excellent chemical stability (see Figure S4a,S5a, and Figure S4b,S5b in the Supporting Information).

To understand the temperature-dependent optical properties of CTC and RTC, low-temperature PL measurements were performed from 50 to 250 K, which is shown in Figure 2d. The PL intensity gradually decreases as a function of temperature due to an increase in the nonradiative recombination centers.²⁹ The exciton binding energies of CTC and RTC are approximately 26.51 and 13.17 meV, respectively (Figure 2e). These values are smaller than those of previously reported metal halides.^{30–32} Furthermore, we also measured the TQ properties of CTC and RTC. Surprisingly, CTC and RTC retained over 90% of their original PL properties at 250 °C (Figure 2f, and Figure S6 in the Supporting Information). They also retained over 90% of their original RL intensity at 250 °C, without phase transitions (Figure S7a–d in the Supporting Information). To further understand the thermal stability of CTC and RTC, a thermogravimetric analysis (TGA) and differential scanning calorimetry (DSC) analysis were conducted (Figure S7e,f in the Supporting Information). The TGA results reveal a negligible mass reduction below 600 °C. Furthermore, their Debye temperatures (Θ_D) were calculated using the quasi-harmonic model to predict their structural rigidity; the Θ_D value is the most reliable descriptor for evaluating structural robustness.³³ The Θ_D values of CTC and RTC were calculated

to be 394 and 452 K, respectively. These values are much higher than those of other 0D metal halides³⁴ and are comparable to those of conventional phosphor hosts, such as Ba_2SiO_4 (307 K),³⁵ Sr_2SiO_4 (360 K),³⁵ and SrSiN_2 (375 K).³⁶ These results suggest that CTC and RTC are thermally stable due to the robustness of their crystal structures.

It should be noted that the emissions of CTC and RTC appear from their Tb^{3+} luminescent centers. Halide perovskite materials generate band edge emission via exciton recombination.³⁷ Therefore, if their exciton binding energy is low, they are considerably affected by TQ at high temperatures.^{38–40} Similarly, most metal halides emitting by self-trapped excitons (STEs) are also much more susceptible to TQ if they have a lower exciton binding energy than metal halides with large exciton binding energy.^{41–43} However, the emissions of CTC and RTC appear from their Tb^{3+} luminescent centers. According to the crossover and thermal-ionization theory, their luminescent center position in the band structure much more dominantly affects thermal quenching than their excitonic nature.^{44–48} Therefore, we assumed that these materials exhibit good scintillation properties due to the low exciton binding energy of the spontaneous free carrier generation under X-ray irradiation, as well as their robust structure.^{49–51}

To investigate the scintillation performance of CTC and RTC, their X-ray absorption coefficients were estimated. The X-ray absorption coefficient is determined primarily by the

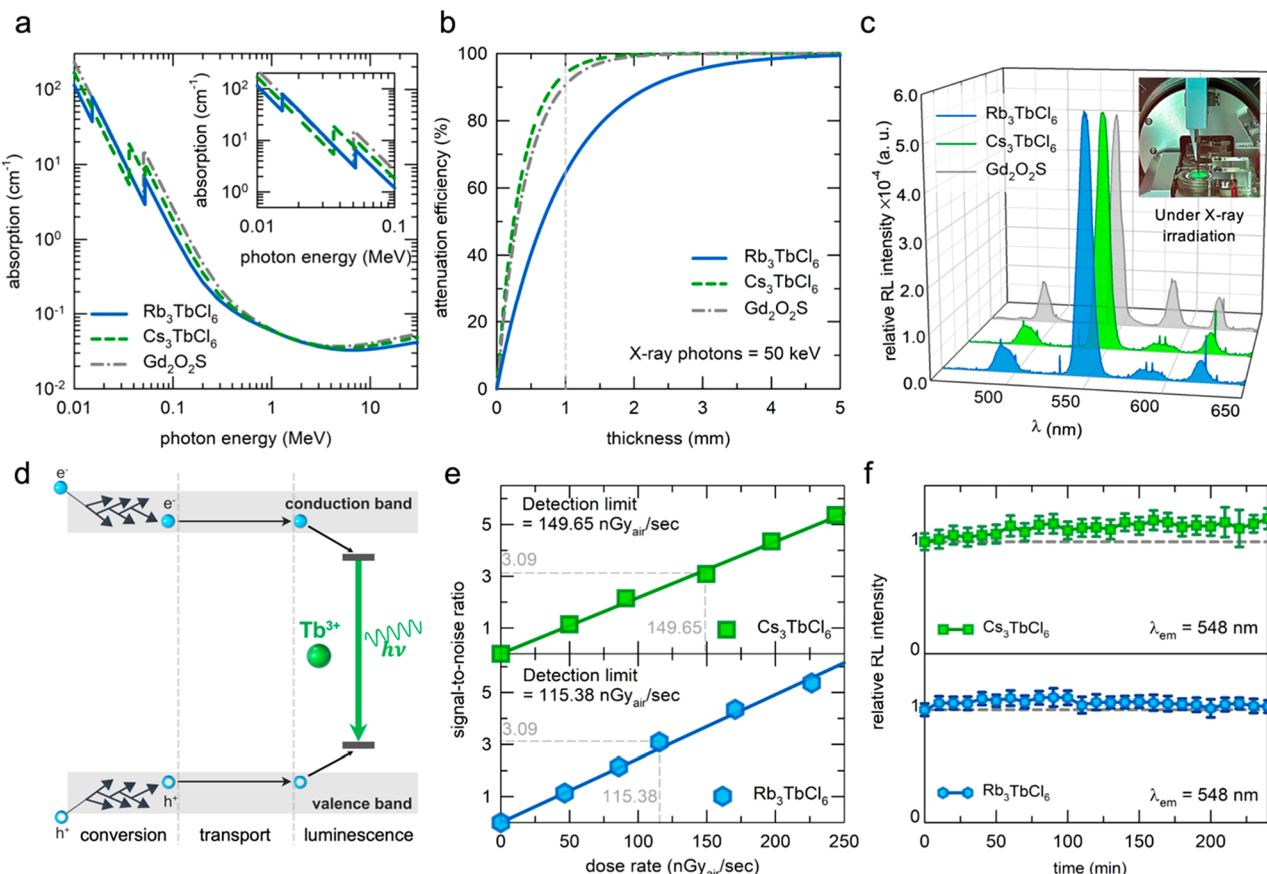


Figure 3. Scintillation performance of CTC and RTC metal halides. (a) Absorption coefficients of CTC, RTC, and a commercial GOS scintillator to X-ray photons, from the variant radiation photon energy. The inset shows a magnified energy scale for fluoroscopy and radiography applications. (b) X-ray attenuation efficiencies of CTC, RTC, and a commercial GOS scintillator as a function of thickness. (c) Radioluminescence (RL) spectrum of CTC, RTC, and GOS scintillators. The inset shows a photograph of RTC polycrystals under X-ray irradiation. (d) Schematic diagram of the scintillator conversion mechanism in CTC and RTC. The process is divided into conversion, transport, and luminescence. (e) The linear response between RL intensity and X-ray dose rate of CTC and RTC under low-dose-rate excitation. Their detection limits can be defined, as the signal to noise ratio (SNR) is 3. (f) RL intensity tracking of CTC and RTC under continuous X-ray irradiation over 4 h (tube voltage, 70 kV; tube current, 50 mA).

effective atomic number (Z_{eff}) and the density (ρ).⁵² The Z_{eff} values of CTC and RTC are 43.07 and 41.13, and their ρ values are 3.55 and 3.18 g/cm³, respectively. The X-ray absorption spectra of CTC and RTC were compared to those of a commercial GOS scintillator for high-energy photons (0.01–30 MeV) (Figure 3a). The X-ray absorption coefficients of CTC and RTC are comparable to those of GOS. Similar trends were observed in the energy range of 0.01–0.1 MeV for radiography applications in mammography.⁵³ Moreover, We also investigated the X-ray attenuation efficiency as a function of thickness, because X-ray imaging applications require thick films ranging from micrometers to millimeters. The X-ray attenuation efficiency spectra under 50 keV (the mean photon energy value of our X-ray tube) of CTC and RTC are shown in Figure 3b. The curve corresponding to CTC is slightly higher than the GOS curve and much higher than the RTC curve, due to their X-ray absorption coefficients. The X-ray attenuation efficiencies of CTC and RTC at a thickness of 1 mm were calculated to be 94.05% and 64.55%, respectively. A photograph of the bright green emissive CTC polycrystals under X-ray irradiation is shown in the inset of Figure 3c. The RL measurements of CTC, RTC, and GOS scintillators were performed at room temperature. The RL spectra were similar to the PL spectra. The relative RL intensity of RTC is higher

than that of CTC, and they have high light yields of 88,800 and 56800 photons/MeV, respectively. These values are much higher than that of CsPbBr_3 , and the light yield of RTC exceeds that of the commercial GOS scintillator.^{54,55} The scintillation process of CTC and RTC is shown in Figure 3d. The scintillation process can be divided into three stages: conversion, transport, and luminescence.⁵⁶ In the conversion stage, due to the photoelectric effect, the scintillator converts incident radiation energy into high-energy electrons and holes. The generated electrons and holes induce secondary electrons and holes. In the transport stage, generated electrons and holes are transferred to the luminescent center. In the luminescence stage, the transferred electrons and holes are recombined at the luminescent center from the excited and ground states to generate light. The high RL performances of CTC and RTC can be explained by the generation of a greater amount of free charge carriers through thermalization due to their low exciton binding energies, which contribute to the strong radiative recombination occurring in their Tb^{3+} luminescent centers.^{6,38}

Furthermore, the linear responses of CTC and RTC were investigated. The RL intensities were measured at different dose rates, as shown in Figure S8 in the Supporting Information. The responses of CTC and RTC are higher than those of GOS. The high linearity between RL intensity

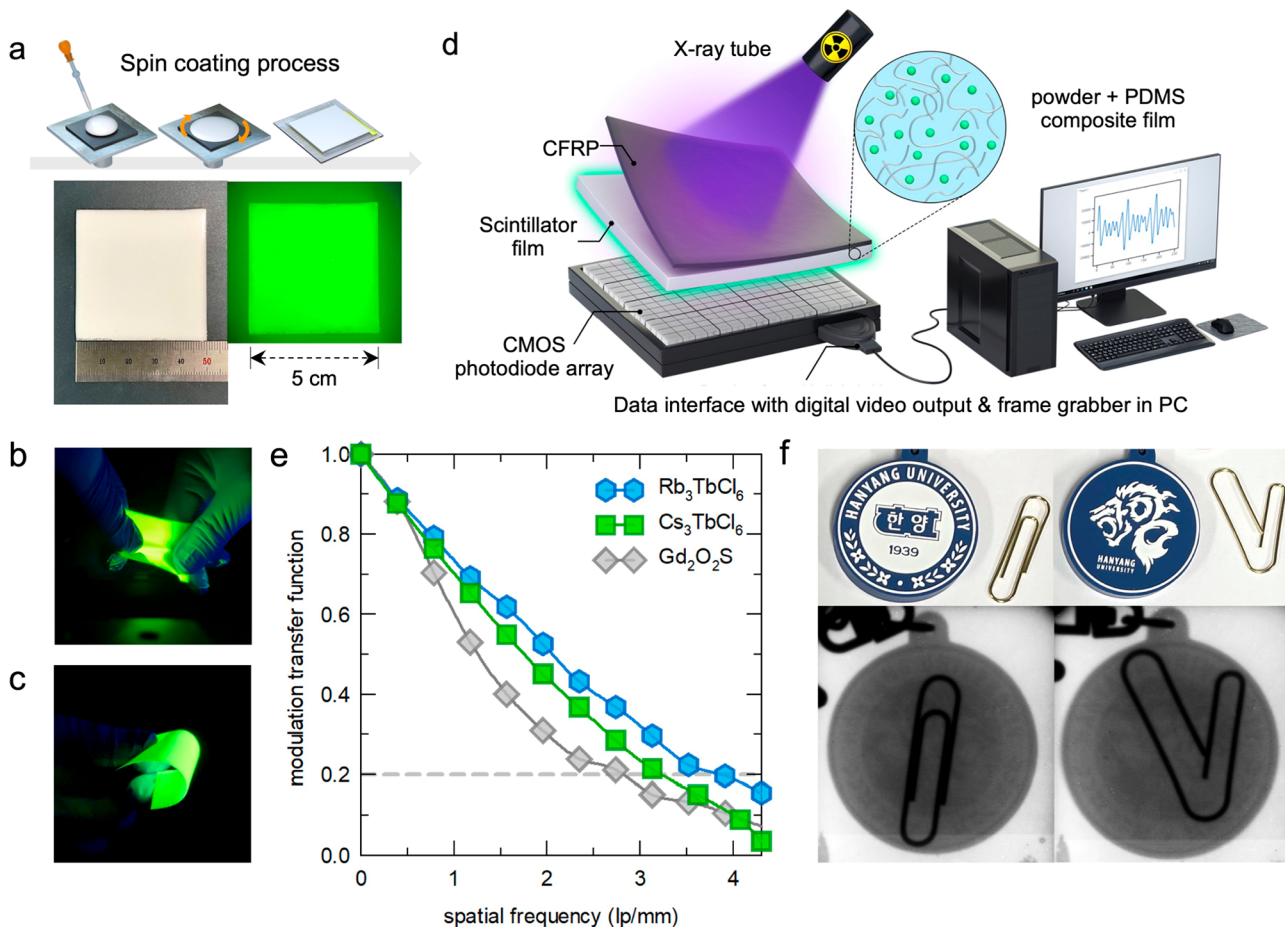


Figure 4. X-ray imaging of CTC and RTC scintillator films. (a) Fabrication method of CTC and RTC scintillator films and photographs of a scintillator film under daylight and a 254 nm UV lamp. (b, c) Photographs of stretched and bent scintillator films, respectively. (d) Device schematic of the X-ray imaging system. (e) Spatial resolution measurement of CTC, RTC, and GOS scintillator films. (f) Photographs of normal (left) and bent (right) clips and a key ring. X-ray images of normal and bent clips under a key-ring using a CTC scintillator film. (Photographs of normal and bent clips and a key ring are shown with permission from Hanyang University. X-ray images of normal and bent clips and a key ring also are shown with permission from Hanyang University.)

and X-ray dose rate under greater dose rate excitation is advantageous for obtaining high contrast in X-ray imaging.²¹ Additionally, the detection limit under a dose rate with a signal to noise ratio (SNR) of 3.09 at low intensity was defined (Figure 3e). The detection limits of CTC and RTC are 149.65 and 115.38 nGyair⁻¹, respectively. These values are lower than that of a CsI scintillator (180 nGyair⁻¹)⁵⁷ and much lower than those required for medical X-ray diagnosis standards.⁵⁸ To investigate the stability under continuous X-ray irradiation, we continuously measured the RL intensity of CTC and RTC over 4 h of continuous X-ray irradiation (Figure 3f). The RL intensities of CTC and RTC do not fall below their initial RL intensities, and they show robust stability under continuous X-ray irradiation.

To apply CTC and RTC to our homemade X-ray imaging system,⁵⁹ thick films of these materials were fabricated. CTC and RTC PCs were mixed with a polydimethylsiloxane (PDMS) binder, following which a spin-coating method was used to fabricate large-area (25 cm^2) films (Figure 4a). The lower images in Figure 4a are photographs of a scintillator film under daylight and under a 254 nm UV lamp in the dark. Due to the high ductility of PDMS, the scintillator films could be well-stretched and well-bent while maintaining homogeneous green emission under a 254 nm UV lamp (Figure 4b,c). As

confirmed from Figure S9 in the Supporting Information, the RL spectra of CTC and RTC matched well with the external quantum efficiency spectrum of the CMOS sensor. Figure 4d shows the schematic device structure of the indirect X-ray detector constructed using CTC and RTC scintillator films. The indirect X-ray detector consists of a carbon-fiber-reinforced polymer (CFRP) film/scintillator film/arranged CMOS photodiode, which acquires X-ray images through a data interface with a digital video output and a frame grabber. Another important indicator of the performance of an X-ray detector is its spatial resolution, which can be determined using the modulation transfer function (MTF). The spatial resolution of the X-ray detector is affected by the spatial resolution of the photodiode array as well as the thickness and performance of the scintillator film. The slanted edge method was used for MTF measurement, and the spatial resolution of the commercial GOS film was measured in the same system as for the CTC and RTC scintillator films (260 μm thickness, Figure S10a in the Supporting Information) to make a comparison (Figure 4e). The spatial resolutions of the CTC and RTC films at the MTF values of 0.2 were 3.3 and 3.9 lp mm⁻¹, respectively. These values are slightly higher than the spatial resolution of the commercial GOS film, as reported in a previous study (2.7 lp mm⁻¹).⁵⁹ Subsequently, static X-ray

imaging was performed using CTC and RTC scintillator films (Figure 4f and Figure S10b in the Supporting Information). As seen in Figure 4f, normal and bent clips cannot be identified by the naked eye if they are under a key-ring. However, they could be clearly distinguished in the obtained X-ray images. Similarly, a clear X-ray image of the structure inside a ballpoint pen could be obtained (Figure S9b in the Supporting Information); these high-contrast X-ray images confirm the excellent X-ray conversion capability of CTC and RTC. It should be noted that, in the fabrication of scintillator films for X-ray imaging, transparency is important.⁶⁰ From this point of view, we also synthesized CTC and RTC in nanocrystalline forms and single crystals (Synthesis in the Supporting Information) which have properties similar to those of polycrystalline phases (detailed characterizations are shown in Figure S11). We will also apply single crystals and nanocrystals for X-ray imaging applications in further research.

In summary, we developed new zero-dimensional lead-free monoclinic CTC and RTC metal halides. The CTC and RTC showed bright green emissions with excellent thermal and chemical stability. Furthermore, CTC and RTC exhibited promising scintillation properties such as high X-ray absorption efficiency, high light yield, low detection limit, and high stability under continuous X-ray irradiation. Subsequently, indirect X-ray detectors were also fabricated using thick CTC and RTC scintillator films as scintillator films. All of the above features enabled a higher spatial resolution for X-ray imaging in comparison with the commercial GOS scintillators. Thus, we believe that the CTC and RTC scintillators can offer new opportunities for effective radiation detection under harsh conditions.

■ ASSOCIATED CONTENT

Data Availability Statement

Research data are not shared.

■ Supporting Information

The Supporting Information is available free of charge at <https://pubs.acs.org/doi/10.1021/acsenergylett.2c02469>.

Experimental details and supplementary characterizations of materials and devices, additional analysis of crystal structures, and the structural and optical properties of nanocrystals and single crystals (PDF)

The X-ray luminescence video of Cs₃TbCl₆ polycrystals (MP4)

■ AUTHOR INFORMATION

Corresponding Authors

Won Bin Im — Division of Materials Science and Engineering, Hanyang University, Seoul 04763, Republic of Korea;  orcid.org/0000-0003-2473-4714; Email: imwonbin@hanyang.ac.kr

Sung Beom Cho — Department of Materials Science and Engineering, Ajou University, Suwon-si 16499, Republic of Korea; Email: csb@ajou.ac.kr

Authors

Joo Hyeong Han — Division of Materials Science and Engineering, Hanyang University, Seoul 04763, Republic of Korea

Tuhin Samanta — Division of Materials Science and Engineering, Hanyang University, Seoul 04763, Republic of Korea

Yong Min Park — Division of Materials Science and Engineering, Hanyang University, Seoul 04763, Republic of Korea

Ha Jun Kim — Division of Materials Science and Engineering, Hanyang University, Seoul 04763, Republic of Korea

Noolu Srinivasa Manikanta Viswanath — Division of Materials Science and Engineering, Hanyang University, Seoul 04763, Republic of Korea

Hyeon Woo Kim — Center of Materials Digitalization, Korea Institute of Ceramic Engineering and Technology (KICET), Jinju-si 52851, Republic of Korea; Division of Materials Science and Engineering, Hanyang University, Seoul 04763, Republic of Korea

Bo Kyung Cha — Precision Medical Device Research Center, Korea Electrotechnology Research Institute (KERI), Ansan 15588, Republic of Korea

Complete contact information is available at:
<https://pubs.acs.org/10.1021/acsenergylett.2c02469>

Notes

The authors declare no competing financial interest.

■ ACKNOWLEDGMENTS

This work was supported by the National Research Foundation of Korea (NRF) grants funded by the Korean government (MSIT) (NRF-2020M3H4A3081792, NRF-2021M3H4A1A02049634, NRF-2022H1D3A3A01077343).

■ REFERENCES

- (1) Cha, B. K.; Kim, J. Y.; Kim, T. J.; Sim, C.; Cho, G. Fabrication and imaging characterization of high sensitive CsI (Tl) and Gd₂O₃ (Tb) scintillator screens for X-ray imaging detectors. *Radiat. Meas.* **2010**, *45* (3–6), 742–745.
- (2) Nagarkar, V.; Gupta, T.; Miller, S.; Klugerman, Y.; Squillante, M.; Entine, G. Structured CsI (Tl) scintillators for X-ray imaging applications. *IEEE Trans. Nucl. Sci.* **1998**, *45* (3), 492–496.
- (3) Qin, L.; Li, H.; Lu, S.; Ding, D.; Ren, G. Growth and characteristics of LYSO (Lu_{2(1-x-y)} Y_xSiO₅: Ce_y) scintillation crystals. *J. Cryst. Growth* **2005**, *281* (2–4), 518–524.
- (4) Zhou, Y.; Chen, J.; Bakr, O. M.; Mohammed, O. F. Metal halide perovskites for X-ray imaging scintillators and detectors. *ACS Energy Letters* **2021**, *6* (2), 739–768.
- (5) Nikl, M.; Yoshikawa, A. Recent R&D trends in inorganic single-crystal scintillator materials for radiation detection. *Adv. Opt. Mater.* **2015**, *3* (4), 463–481.
- (6) Starkenburg, D. J.; Johns, P. M.; Baciaik, J. E.; Nino, J. C.; Xue, J. Thin film organic photodetectors for indirect X-ray detection demonstrating low dose rate sensitivity at low voltage operation. *J. Appl. Phys.* **2017**, *122* (22), 225502.
- (7) Weber, M. J. Inorganic scintillators: today and tomorrow. *J. Lumin.* **2002**, *100* (1–4), 35–45.
- (8) Grandhi, G. K.; Kim, H. J.; Viswanath, N.; Cho, H. B.; Han, J. H.; Kim, S. M.; Im, W. B. Strategies for improving luminescence efficiencies of blue-emitting metal halide perovskites. *J. Korean Ceram. Soc.* **2021**, *58* (1), 28–41.
- (9) Jang, J.; Ji, S.; Grandhi, G. K.; Cho, H. B.; Im, W. B.; Park, J. U. Multimodal Digital X-ray Scanners with Synchronous Mapping of Tactile Pressure Distributions using Perovskites. *Adv. Mater.* **2021**, *33* (30), 2008539.
- (10) Matt, G. J.; Levchuk, I.; Knüttel, J.; Dallmann, J.; Osvet, A.; Sytnyk, M.; Tang, X.; Elia, J.; Hock, R.; Heiss, W.; et al. Sensitive Direct Converting X-Ray Detectors Utilizing Crystalline CsPbBr₃ Perovskite Films Fabricated via Scalable Melt Processing. *Adv. Mater. Interfaces* **2020**, *7* (4), 1901575.
- (11) Stoumpos, C. C.; Malliakas, C. D.; Peters, J. A.; Liu, Z.; Sebastian, M.; Im, J.; Chasapis, T. C.; Wibowo, A. C.; Chung, D. Y.;

- Freeman, A. J.; et al. Crystal growth of the perovskite semiconductor CsPbBr_3 : a new material for high-energy radiation detection. *Cryst. Growth Des.* **2013**, *13* (7), 2722–2727.
- (12) Wang, J.-X.; Wang, X.; Yin, J.; Gutiérrez-Arzaluz, L.; He, T.; Chen, C.; Han, Y.; Zhang, Y.; Bakr, O. M.; Eddaoudi, M.; et al. Perovskite-nanosheet sensitizer for highly efficient organic X-ray imaging scintillator. *ACS Energy Letters* **2022**, *7* (1), 10–16.
- (13) Dong, Y.; Parobek, D.; Son, D. H. Controlling quantum confinement and magnetic doping of cesium lead halide perovskite nanocrystals. *J. Korean Ceram. Soc.* **2018**, *55* (6), 515–526.
- (14) Grandhi, G. K.; Mokurala, K.; Han, J. H.; Bin Cho, H.; Han, J. Y.; Im, W. B. Recent Advances and Challenges in Obtaining Stable CsPbX_3 ($X = \text{Cl}$, Br , and I) Nanocrystals Toward White Light-Emitting Applications. *ECS J. Solid State Sci. Technol.* **2021**, *10* (10), 106001.
- (15) Heo, J. H.; Shin, D. H.; Park, J. K.; Kim, D. H.; Lee, S. J.; Im, S. H. High-performance next-generation perovskite nanocrystal scintillator for nondestructive X-ray imaging. *Adv. Mater.* **2018**, *30* (40), 1801743.
- (16) Ren, X.; Jung, H. S. Recent progress in flexible perovskite solar cell development. *J. Korean Ceram. Soc.* **2018**, *55* (4), 325–336.
- (17) He, T.; Zhou, Y.; Wang, X.; Yin, J.; Gutiérrez-Arzaluz, L.; Wang, J.-X.; Zhang, Y.; Bakr, O. M.; Mohammed, O. F. High-Performance Copper-Doped Perovskite-Related Silver Halide X-ray Imaging Scintillator. *ACS Energy Letters* **2022**, *7* (8), 2753–2760.
- (18) Zhou, Y.; Wang, X.; He, T.; Yang, H.; Yang, C.; Shao, B.; Gutiérrez-Arzaluz, L.; Bakr, O. M.; Zhang, Y.; Mohammed, O. F. Large-Area Perovskite-Related Copper Halide Film for High-Resolution Flexible X-ray Imaging Scintillation Screens. *ACS Energy Letters* **2022**, *7* (2), 844–846.
- (19) Yang, B.; Yin, L.; Niu, G.; Yuan, J. H.; Xue, K. H.; Tan, Z.; Miao, X. S.; Niu, M.; Du, X.; Song, H.; et al. Lead-Free Halide Rb_2CuBr_3 as Sensitive X-Ray Scintillator. *Adv. Mater.* **2019**, *31* (44), 1904711.
- (20) Zhang, M.; Wang, X.; Yang, B.; Zhu, J.; Niu, G.; Wu, H.; Yin, L.; Du, X.; Niu, M.; Ge, Y.; et al. Metal Halide Scintillators with Fast and Self-Absorption-Free Defect-Bound Excitonic Radioluminescence for Dynamic X-Ray Imaging. *Adv. Funct. Mater.* **2021**, *31* (9), 2007921.
- (21) Jiang, T.; Ma, W.; Zhang, H.; Tian, Y.; Lin, G.; Xiao, W.; Yu, X.; Qiu, J.; Xu, X.; Yang, Y.; et al. Highly Efficient and Tunable Emission of Lead-Free Manganese Halides toward White Light-Emitting Diode and X-Ray Scintillation Applications. *Adv. Funct. Mater.* **2021**, *31* (14), 2009973.
- (22) Ou, X.; Qin, X.; Huang, B.; Zan, J.; Wu, Q.; Hong, Z.; Xie, L.; Bian, H.; Yi, Z.; Chen, X.; et al. High-resolution X-ray luminescence extension imaging. *Nature* **2021**, *590* (7846), 410–415.
- (23) Liu, Y.; Rong, X.; Li, M.; Molokeev, M. S.; Zhao, J.; Xia, Z. Incorporating Rare-Earth Terbium (III) Ions into $\text{Cs}_2\text{AgInCl}_6:\text{Bi}$ Nanocrystals toward Tunable Photoluminescence. *Angew. Chem., Int. Ed.* **2020**, *59* (28), 11634–11640.
- (24) Nikl, M. Scintillation detectors for X-rays. *Measurement Science and Technology* **2006**, *17* (4), R37.
- (25) Kubelka, P. Ein Beitrag zur Optik der Farbanstriche (Contribution to the optic of paint). *Z. Technol. Physik* **1931**, *12*, 593–601.
- (26) Tauc, J.; Grigorovici, R.; Vancu, A. Optical properties and electronic structure of amorphous germanium. *Phys. Status Solidi B* **1966**, *15* (2), 627–637.
- (27) Cavalli, E.; Boutinaud, P.; Mahiou, R.; Bettinelli, M.; Dorenbos, P. Luminescence dynamics in Tb^{3+} -doped CaWO_4 and CaMoO_4 crystals. *Inorg. Chem.* **2010**, *49* (11), 4916–4921.
- (28) Joos, J. J.; Van der Heggen, D.; Martin, L. I.; Amidani, L.; Smet, P. F.; Barandiarán, Z.; Seijo, L. Broadband infrared LEDs based on europium-to-terbium charge transfer luminescence. *Nat. Commun.* **2020**, *11* (1), 1–11.
- (29) Viswanath, N.; Arunkumar, P.; Kim, H. J.; Im, W. B. A nanosheet phosphor of double-layered perovskite with unusual intranasheet site activator concentration. *Chem. Eng. J.* **2019**, *375*, 122044.
- (30) Chen, Q.; Wu, J.; Ou, X.; Huang, B.; Almutlaq, J.; Zhumeenov, A. A.; Guan, X.; Han, S.; Liang, L.; Yi, Z.; et al. All-inorganic perovskite nanocrystal scintillators. *Nature* **2018**, *561* (7721), 88–93.
- (31) Grandhi, G. K.; Viswanath, N.; Cho, H. B.; Han, J. H.; Kim, S. M.; Choi, S.; Im, W. B. Mechanochemistry as a green route: Synthesis, thermal stability, and postsynthetic reversible phase transformation of highly-luminescent cesium copper halides. *J. Phys. Chem. Lett.* **2020**, *11* (18), 7723–7729.
- (32) Zheng, K.; Chen, B.; Xie, L.; Li, X.; Lu, B.; Wang, M.; Wu, Y.; Jiang, T.; Zhang, F.; Li, X.; et al. Vacancy-Ordered Double Perovskite $\text{Rb}_2\text{ZrCl}_{6-x}\text{Br}_x$: Facile Synthesis and Insight into Efficient Intrinsic Self-Trapped Emission. *Adv. Opt. Mater.* **2022**, *10* (2), 2101661.
- (33) Zhuo, Y.; Mansouri Tehrani, A.; Oliynyk, A. O.; Duke, A. C.; Brigo, J. Identifying an efficient, thermally robust inorganic phosphor host via machine learning. *Nat. Commun.* **2018**, *9* (1), 1–10.
- (34) Hu, M.; Ge, C.; Yu, J.; Feng, J. Mechanical and optical properties of Cs_3BX_6 ($\text{B} = \text{Pb}, \text{Sn}$; $\text{X} = \text{Cl}, \text{Br}, \text{I}$) zero-dimension perovskites. *J. Phys. Chem. C* **2017**, *121* (48), 27053–27058.
- (35) Ha, J.; Wang, Z.; Novitskaya, E.; Hirata, G. A.; Graeve, O. A.; Ong, S. P.; McKittrick, J. An integrated first principles and experimental investigation of the relationship between structural rigidity and quantum efficiency in phosphors for solid state lighting. *J. Lumin.* **2016**, *179*, 297–305.
- (36) Wang, Z.; Chu, I.-H.; Zhou, F.; Ong, S. P. Electronic structure descriptor for the discovery of narrow-band red-emitting phosphors. *Chem. Mater.* **2016**, *28* (11), 4024–4031.
- (37) Herz, L. M. Charge-carrier dynamics in organic-inorganic metal halide perovskites. *Annu. Rev. Phys. Chem.* **2016**, *67* (1), 65–89.
- (38) Birowosuto, M.; Cortecchia, D.; Drozdowski, W.; Brylew, K.; Lachmanski, W.; Bruno, A.; Soci, C. X-ray scintillation in lead halide perovskite crystals. *Sci. Rep.* **2016**, *6* (1), 1–10.
- (39) Peters, J. A.; Liu, Z.; Michael, C.; Kanatzidis, M. G.; Wessels, B. W. Photoluminescence spectroscopy of excitonic emission in CsPbCl_3 perovskite single crystals. *J. Lumin.* **2022**, *243*, 118661.
- (40) Lao, X.; Yang, Z.; Su, Z.; Wang, Z.; Ye, H.; Wang, M.; Yao, X.; Xu, S. Luminescence and thermal behaviors of free and trapped excitons in cesium lead halide perovskite nanosheets. *Nanoscale* **2018**, *10* (21), 9949–9956.
- (41) Correa-Baena, J.-P.; Nienhaus, L.; Kurchin, R. C.; Shin, S. S.; Wieghold, S.; Putri Hartono, N. T.; Layurova, M.; Klein, N. D.; Poindexter, J. R.; Polizzotti, A.; et al. A-Site Cation in Inorganic $\text{A}_3\text{Sb}_2\text{I}_9$ Perovskite Influences Structural Dimensionality, Exciton Binding Energy, and Solar Cell Performance. *Chem. Mater.* **2018**, *30* (11), 3734–3742.
- (42) Zhang, G.; Wang, D.; Lou, B.; Ma, C.-G.; Meijerink, A.; Wang, Y. Efficient Broadband Near-Infrared Emission from Lead-Free Halide Double Perovskite Single Crystal. *Angew. Chem., Int. Ed.* **2022**, *61* (33), No. e202207454.
- (43) Luo, J.; Wang, X.; Li, S.; Liu, J.; Guo, Y.; Niu, G.; Yao, L.; Fu, Y.; Gao, L.; Dong, Q.; et al. Efficient and stable emission of warm-white light from lead-free halide double perovskites. *Nature* **2018**, *563* (7732), 541–545.
- (44) Moses, W.; Bizarri, G.; Williams, R. T.; Payne, S.; Vasil'Ev, A.; Singh, J.; Li, Q.; Grim, J.; Choong, W.-S. The origins of scintillator non-proportionality. *IEEE Trans. Nucl. Sci.* **2012**, *59* (5), 2038–2044.
- (45) Blasse, G.; Grabmaier, B. A general introduction to luminescent materials. In *Luminescent materials*; Springer: 1994; pp 1–9.
- (46) Blasse, G.; Bril, A. Characteristic luminescence. *Philips technical review* **1970**, *31* (10), 303.
- (47) Amachraa, M.; Wang, Z.; Chen, C.; Hariyani, S.; Tang, H.; Brigo, J.; Ong, S. P. Predicting thermal quenching in inorganic phosphors. *Chem. Mater.* **2020**, *32* (14), 6256–6265.
- (48) Struck, C.; Fonger, W. Thermal Quenching of Tb^{3+} , Tm^{3+} , Pr^{3+} , and Dy^{3+} $4f_n$ Emitting States in $\text{La}_2\text{O}_2\text{S}$. *J. Appl. Phys.* **1971**, *42* (11), 4515–4516.

- (49) Gao, Z.; Chen, S.; Bai, Y.; Wang, M.; Liu, X.; Yang, W.; Li, W.; Ding, X.; Yao, J. A new perspective for evaluating the photoelectric performance of organic-inorganic hybrid perovskites based on the DFT calculations of excited states. *Phys. Chem. Chem. Phys.* **2021**, *23* (19), 11548–11556.
- (50) Kallatt, S.; Umesh, G.; Bhat, N.; Majumdar, K. Photoresponse of atomically thin MoS₂ layers and their planar heterojunctions. *Nanoscale* **2016**, *8* (33), 15213–15222.
- (51) Rodnyi, P. A. *Physical processes in inorganic scintillators*; CRC Press: 1997; Vol. 14.
- (52) Murty, R. Effective atomic numbers of heterogeneous materials. *Nature* **1965**, *207* (4995), 398–399.
- (53) Datta, A.; Zhong, Z.; Motakef, S. A new generation of direct X-ray detectors for medical and synchrotron imaging applications. *Sci. Rep.* **2020**, *10* (1), 1–10.
- (54) Lecoq, P. Development of new scintillators for medical applications. *Nucl. Instrum. Methods Phys. Res. A: Accel. Spectrom. Detect. Assoc. Equip.* **2016**, *809*, 130–139.
- (55) Zhu, W.; Ma, W.; Su, Y.; Chen, Z.; Chen, X.; Ma, Y.; Bai, L.; Xiao, W.; Liu, T.; Zhu, H.; et al. Low-dose real-time X-ray imaging with nontoxic double perovskite scintillators. *Light Sci. Appl.* **2020**, *9* (1), 1–10.
- (56) Blasse, G. Scintillator materials. *Chem. Mater.* **1994**, *6* (9), 1465–1475.
- (57) Feng, H.; Jary, V.; Mihokova, E.; Ding, D.; Nikl, M.; Ren, G.; Li, H.; Pan, S.; Beitlerova, A.; Kucerkova, R. Temperature dependence of luminescence characteristics of Lu_{2(1-x)}Y_xSiO₅:Ce³⁺ scintillator grown by the Czochralski method. *J. Appl. Phys.* **2010**, *108* (3), 033519.
- (58) Wei, H.; Fang, Y.; Mulligan, P.; Chuirazzi, W.; Fang, H.-H.; Wang, C.; Ecker, B. R.; Gao, Y.; Loi, M. A.; Cao, L.; et al. Sensitive X-ray detectors made of methylammonium lead tribromide perovskite single crystals. *Nat. Photonics* **2016**, *10* (5), 333–339.
- (59) Cha, B. K.; Jeon, S.; Seo, C.-W. X-ray performance of a wafer-scale CMOS flat panel imager for applications in medical imaging and nondestructive testing. *Nucl. Instrum. Methods Phys. Res. A: Accel. Spectrom. Detect. Assoc. Equip.* **2016**, *831*, 404–409.
- (60) Han, K.; Sakhatskyi, K.; Jin, J.; Zhang, Q.; Kovalenko, M. V.; Xia, Z. Seed-Crystal-Induced Cold Sintering Toward Metal Halide Transparent Ceramic Scintillators. *Adv. Mater.* **2022**, *34* (17), 2110420.

□ Recommended by ACS

Copper Organometallic Iodide Arrays for Efficient X-ray Imaging Scintillators

Hong Wang, Omar F. Mohammed, *et al.*

MARCH 10, 2023

ACS CENTRAL SCIENCE

READ ▶

Gamma-Ray Irradiation Stability of Zero-Dimensional Cs₃Cu₂I₅ Metal Halide Scintillator Single Crystals

Lei Gao, Qingfeng Yan, *et al.*

JANUARY 30, 2023

THE JOURNAL OF PHYSICAL CHEMISTRY LETTERS

READ ▶

Fabrication of a Large-Area Flexible Scintillating Membrane for High-Resolution X-ray Imaging Using an AIEgen-Functionalized Metal–Organic Framework

Lilin Zhang, Wei Liu, *et al.*

APRIL 11, 2023

INORGANIC CHEMISTRY

READ ▶

Cryogenic Scintillation Properties of Lead-Free Cs₃Cu₂I₅ Single Crystals

Bo Liu, Xiaoping Ouyang, *et al.*

SEPTEMBER 23, 2022

INORGANIC CHEMISTRY

READ ▶

Get More Suggestions >